AIAA JOURNAL
Vol. 49, No. 12, December 2011

Computation of Aircraft Stability Derivatives Using an Automatic Differentiation Adjoint Approach

Charles A. Mader*
University of Toronto, Toronto, Ontario M3H 5T6, Canada
and
Joaquim R. R. A. Martins†
University of Michigan, Ann Arbor, Michigan 48109

DOI: 10.2514/1.J051147

This paper presents a method for the computation of the static and dynamic stability derivatives of arbitrary aircraft configurations. Three-dimensional computational fluid dynamics are used in this method to simulate the flow characteristics around the configuration, and a moving-grid formulation is included in the flow solver to handle the rotational physics necessary for the computation of the dynamic derivatives. To obtain the stability derivatives, the computational fluid dynamics code is differentiated using the automatic differentiation adjoint (ADjoint) approach. This approach enables the efficient and accurate computation of derivatives for a wide variety of variables, including the dynamic model states that are typical of the stability derivatives. To demonstrate the effectiveness of this approach, stability derivatives are computed for a NACA 0012 airfoil and an ONERA M6 wing.

Nomenclature

b	=	span
C_D	=	aircraft drag coefficient
C_L	=	aircraft lift coefficient
C_l	=	airfoil lift coefficient (Sec. III.B), aircraft roll moment coefficient (Sec. IV)
C_m	=	airfoil pitch moment coefficient (Sec. III.B), aircraft pitch moment coefficient (Sec. IV)
C_n	=	aircraft yaw moment coefficient
C_p	=	coefficient of pressure
C_Y	=	aircraft side force coefficient
c	=	chord
e_t	=	total energy
f	=	flux term
h	=	altitude
I	=	identity matrix (Sec. III.A), function of interest (Sec. III.C)
k	=	thermal conductivity of fluid
M	=	Mach number
N	=	number of surface cells (PMARC), number of volume cells (SUmb)
p	=	pressure (Sec. III.A), roll rate (Sec. III.C), order of convergence (Sec. IV.A)
$\hat{p}$	=	normalized roll rate ($pb/2V$)
q	=	pitch rate
$\hat{q}$	=	normalized pitch rate ($qc/2V$)
$\mathcal{R}$	=	flow residuals
r	=	yaw rate
$\hat{r}$	=	normalized yaw rate ($rb/2V$)
s	=	source terms
T	=	temperature
t	=	time
u	=	flow velocity with respect to the fixed frame
v	=	flow velocity with respect to the moving grid
V	=	aircraft speed
w	=	velocity of the moving grid
x	=	grid coordinates (Sec. III.A), design variables (Sec. III.C)
x_{ref}	=	center of moment and rotation with respect to wing root/airfoil leading edge
α	=	angle of attack
β	=	sideslip angle
δ_i	=	ith control surface deflection (Sec. III.C), elements of the identity matrix (Sec. III.A)
ζ	=	flow states
ρ	=	density
σ	=	viscous stress tensor
τ	=	generalized time variable
Ψ	=	adjoint vector
Ω	=	rotational rate of the moving grid

Received 27 December 2010; revision received 31 March 2011; accepted for publication 17 April 2011.

*Ph.D. Candidate, Institute for Aerospace Studies. Student Member AIAA.

†Associate Professor, Department of Aerospace Engineering. Senior Member AIAA.

I. Introduction

FLIGHT dynamic characteristics are an essential factor in aircraft design. However, due to the unsteady nature of the flow around the aircraft during maneuvers, it is extremely challenging to determine the aerodynamic characteristics of aircraft for flight dynamics purposes. One common way to make this problem more tractable is to assume that the aerodynamic forces on the aircraft react in a linear fashion for small variations from a given steady-state flight condition. This assumption allows the forces to be characterized by a series of aerodynamic derivatives, typically called *stability derivatives* [1]. These derivatives can be calculated using empirical methods (e.g., DATCOM [2] and ESDU [3,4]), wind-tunnel testing, or computational fluid dynamics (CFD). Each of these approaches has its own advantages and disadvantages with respect to cost, range of applicability, and computational time. In this work, we seek to use adjoint methods and automatic differentiation to remove some of the barriers limiting the use of high-fidelity CFD for these computations.

II. Background

The task of computing aerodynamic information for stability and control purposes remains a difficult challenge for aircraft designers. This difficulty is especially acute in the early stages of the design process, when detailed information about the design is less certain. There are several well-documented cases, even for relatively modern aircraft such as the Boeing 777 and the Learjet 23, in which stability and control problems were not diagnosed until the flight-test

stage of the design, resulting in costly late-stage modifications to the aircraft [5].

CFD has been identified as a tool that may be able to address these issues, since it can give a better understanding of the stability and control characteristics of a proposed configuration at various stages of the design. Some CFD-based methods have already made inroads into this area of analysis. For example, according to Johnson et al. [6], Boeing uses their A502 panel code to compute stability derivatives at the preliminary design stage. However, while the methods currently in use provide rapid turnaround times and provide useful results for a wide variety of cases, they still have some significant limitations, which have diminished their general acceptance for use in stability and control. As demonstrated by the COMSAC working group [5], in order for CFD to truly be accepted in stability and control prediction, it must be able to handle computations for the full flight envelope, including flight conditions exhibiting massive flow separation, which often occur at the edges of the flight envelope. In the working group's opinion, to accurately predict the flow for these difficult flight conditions, higher-fidelity CFD methods are needed, such as Reynolds-averaged Navier–Stokes (RANS), large eddy simulation, or detached eddy simulation (DES).

Considering this outlook, we can divide the problem of computing stability and control information from CFD into two parts: the task of developing CFD methods to the point where they accurately and robustly model the flows necessary to examine the entire flight envelope, and the task of developing computational techniques to compute usable stability and control information from these solutions efficiently. In this paper, we focus on the second of these two tasks.

Toward this end, many scholars have used a variety of techniques to compute stability and control information using CFD. Charlton [7] conducted simple α and β sweeps to obtain the force and moment information required for falling-leaf predictions for tailless aircraft. The study concluded that, in most instances, the required stability data could be computed accurately, but also that highly nonlinear regions of the flow incurred a large computational cost. Godfrey and Cliff [8] explored the use of analytic sensitivity methods (in particular, the direct method) for the computation of static stability derivatives. They computed the α and β derivatives for the YB-48 flying wing using a three-dimensional inviscid flow solver. They achieved good accuracy, but no comments were made on computational efficiency. Limache and Cliff [9] followed up this work by examining the use of the same method for the computation of dynamic stability derivatives. They showed the computation of the dynamic pitching derivatives of an airfoil using a two-dimensional Euler CFD code. This study showed the promise of analytic sensitivity methods for the computation of stability derivatives and demonstrated that multiple stability derivatives, including the rotational derivatives, could be computed from a single steady solution. The study also highlighted the importance of using, at a minimum, Euler CFD to model the shock waves present in transonic flow. The task of extending this method to a three-dimensional RANS flow solver is not easy and would be a significant barrier to the general adoption of this method.

Another avenue that has been pursued is the use of automatic differentiation to compute stability derivatives. Park et al. [10,11] applied ADIFOR [12], an automatic differentiation tool, to a three-dimensional viscous flow solver to compute the static and dynamic derivatives of various configurations. The results from this work showed promise, providing accurate results across a variety of flight conditions. However, the computational cost of running the differentiated code to compute derivatives with respect to five independent states (α, β, p, q, and r) was equivalent to eight flow solutions. Green et al. [13,14] applied a similar technique to the PMARC panel code. This work focused on the development of techniques, such as uncertainty propagation and derivative separation, so the results are of little direct relevance to the current study.

The previous two approaches to dynamic derivative computation (those of Limache and Cliff [9] and Park et al.[10,11]) relied on a noninertial reference frame CFD formulation to handle the rotational rates needed for the dynamic derivatives. Babcock and Arena [15] handled the dynamic derivatives by modifying the boundary conditions in a finite-element-based Euler CFD solver to separate the velocity and position boundary conditions. With this approach, they were able to perturb the static states (α, β) and the dynamic states (p, q, r) independently to determine the stability derivatives using finite differences. The results from this approach compare relatively well with theoretical, empirical, and experimental results, confirming the validity of the method. However, no details on computational cost are included in the study.

Another way of computing the dynamic derivatives, one that has been used in the experimental community for many years, is the forced-oscillation approach. There has been a recent resurgence in interest in this technique, as it can be used with CFD. A number of papers from the recent NATO RTO Task Group AVT-161 have explored the use of forced-oscillation techniques with a variety of CFD solvers [16], including RANS [17,18], DES [19,20], and harmonic balance [21] solvers. The results in these papers were shown to correlate well with experimental data.

Murman [22] also presented a method for computing stability derivatives based on the traditional forced-oscillation approach. He used a frequency-domain method to produce periodic data for the forced oscillation of the configuration of interest. The data were then analyzed with the same techniques used to produce stability derivatives from forced-oscillation wind-tunnel data, which allowed the method to take advantage of the large body of knowledge in that field. Murman's study demonstrated good accuracy for a variety of configurations and flight conditions. However, because of the time periodic nature of the solution, the computational cost was higher than for an equivalent steady-state solution of the same configuration.

The work presented here builds on the work of Limache and Cliff [9] and Park et al. [10,11]. We apply the automatic differentiation adjoint (ADjoint) approach, which we previously developed [23], to a moving-grid CFD formulation (which is equivalent to the noninertial formulation used by both Limache and Cliff [9] and Park et al. [10,11]) to compute the stability derivatives. As in the previous work of those authors, this CFD formulation allows both the static and dynamic derivatives to be computed from a single steady flow solution. The main advantages of this approach are that it combines the computational efficiency of analytic sensitivity methods with the relatively straightforward implementation of automatic differentiation. This enables the rapid development of an efficient method for the computation of stability derivatives. As we will show, we are able to compute a complete set of static and dynamic stability derivatives for roughly seven times the cost of a single steady flow solution. Note that while the current method is implemented for the Euler equations, the extension to the RANS equations does not require significant new insights. Given the nature of our approach, the inclusion of the RANS terms is a straightforward extension of the presented method.

III. Theory

The stability derivative formulation described in this work is based on two key components. The first is a CFD code that can compute solutions for rotating geometries. This can be accomplished with either a noninertial reference frame formulation or a moving-grid formulation. The moving-grid formulation is used in this work and will be discussed in Sec. III.A; The noninertial formulation can be found in Limache and Cliff [9] or and Park and Green [11]. The second key component of the stability derivative formulation is an efficient, robust, and accurate sensitivity analysis method for the CFD. In our case, this comes in the form of the ADjoint method. A brief summary of this method is provided in Sec. III.C, with more details available in previous work by the authors [23].

A. CFD for Rotating Geometries

In this research, our goal is to compute the derivatives for a given configuration from a single flow solution. To acccomplish this for both static (α, β, V) and dynamic (p, q, r) parameters, we need a flow solver that can compute steady-state solutions for constant,

nonzero values of each of the parameters. Most CFD solvers can perform this computation for a range of static parameters, but few CFD solvers can handle nonzero dynamic parameters.

To handle nonzero dynamic parameters we use a moving-grid formulation. The flow solution is computed using the global velocities as the states. These velocities are expressed in terms of the moving-grid base vectors. This transformation introduces additional terms into the governing equations that account for the moving coordinates of the grid, and eliminates the need to add the centripetal and Coriolis forces as source terms in the momentum equations, as required in the noninertial formulation. The moving-grid formulation is derived below.

1. *Moving-Grid Formulation*

To begin, we define three velocities, u, v, and w, such that

$$u = v + w \tag{1}$$

where u is the velocity of the fluid in the fixed frame, v is the velocity of the fluid with respect to the moving grid, and w is the velocity of the moving grid. Using the approach of Warsi [24], we can write a general form of the conservation law in moving coordinates as

$$\frac{\partial A}{\partial \tau} - (\nabla A)\cdot w + \nabla \cdot F = C \tag{2}$$

where, for the conservation of mass, momentum, and energy, F takes the form $F = Au + B$, and A, B, C and τ can represent various quantities, depending on which quantity is being conserved. In addition, from Warsi [24], we have the identity,

$$\nabla \cdot (Aw) = (\nabla A)\cdot w + A(\nabla \cdot w) \tag{3}$$

which can be derived by applying the product rule to the left-hand side and rearranging the components. This identity can then be rearranged as follows:

$$(\nabla A)\cdot w = \nabla \cdot (Aw) - A(\nabla \cdot w) \tag{4}$$

Using this relationship in the conservation law (2), we can write

$$\frac{\partial A}{\partial \tau} - \nabla \cdot (Aw) + A(\nabla \cdot w) + \nabla \cdot F = C \tag{5}$$

Now substituting F as defined above, we get

$$\frac{\partial A}{\partial \tau} - \nabla \cdot (Aw) + A(\nabla \cdot w) + \nabla \cdot (Au + B) = C \tag{6}$$

Rearranging the above equation, we obtain

$$\frac{\partial A}{\partial \tau} + \nabla \cdot (Au - Aw) + A(\nabla \cdot w) + \nabla \cdot (B) = C \tag{7}$$

Since $(\nabla \cdot w) = 0$, i.e., the grid is incompressible, this equation simplifies to

$$\frac{\partial A}{\partial \tau} + \nabla \cdot (Au - Aw) + \nabla \cdot (B) = C \tag{8}$$

Following the work of Warsi [24] and Ghosh [25], we can then use this conservation equation for mass, momentum, and energy as follows:

a. Mass Conservation. For mass conservation, $A = \rho$, $B = 0$, $C = 0$, and $\tau = t$. This yields

$$\frac{\partial \rho}{\partial t} + \nabla \cdot (\rho u - \rho w) + \nabla \cdot (0) = 0 \tag{9}$$

which can be simplified to

$$\frac{\partial \rho}{\partial t} + \nabla \cdot (\rho(u - w)) = 0 \tag{10}$$

b. Momentum Conservation. In this case, $A = \rho u$, $B = pI - \sigma$, $C = 0$, and $\tau = t$, which yields

$$\frac{\partial \rho u}{\partial t} + \nabla \cdot (\rho u \otimes u - \rho u \otimes w) + \nabla \cdot (pI - \sigma) = 0 \tag{11}$$

Rearranging this equation, we obtain

$$\frac{\partial \rho u}{\partial t} + \nabla \cdot (\rho u \otimes u - \rho u \otimes w + pI - \sigma) = 0 \tag{12}$$

Up to this point, the derivation has been general. Now we cast it in the specific moving-grid base vectors to obtain

$$\frac{\partial \rho u^i}{\partial t} a_i + \rho u^i \frac{\partial a_i}{\partial t} + \nabla \cdot (\rho u \otimes u - \rho u \otimes w + pI - \sigma) = 0 \tag{13}$$

Since it can be shown that $\partial a_i/\partial t - \partial w/\partial x^i = 0$, we can write

$$\frac{\partial \rho u^i}{\partial t} a_i + \rho u^i \frac{\partial w}{\partial x^i} + \nabla \cdot (\rho u \otimes u - \rho u \otimes w + pI - \sigma) = 0 \tag{14}$$

Furthermore, if we let $w = \Omega \times x$, it can be shown that $\rho u^i \partial w/\partial x^i = \rho(\omega \times u)$, and therefore in the moving-grid coordinate system the momentum equations are

$$\frac{\partial \rho u^i}{\partial t} a_i + \nabla \cdot (\rho u \otimes u - \rho u \otimes w + pI - \sigma) + \rho(\omega \times u) = 0 \tag{15}$$

c. Energy Conservation. To obtain the energy conservation equations, we set $A = \rho e_t$, $B = (pI - \sigma)\cdot u + k\nabla T$, $C = 0$ and $\tau = t$, which yields

$$\frac{\partial \rho e_t}{\partial t} + \nabla \cdot (\rho e_t u - \rho e_t w) + \nabla \cdot ((pI - \sigma)\cdot u + k\nabla T) = 0 \tag{16}$$

Rearranging this equation, we obtain

$$\frac{\partial \rho e_t}{\partial t} + \nabla \cdot (\rho e_t u - \rho e_t w + (pI - \sigma)\cdot u + k\nabla T) = 0 \tag{17}$$

where the total energy is given by $e_t = p/(\gamma - 1) + 1/2\rho|u|^2$.

d. Final Formulation. Combining Eqs. (10), (15), and (17) yields the following set of governing equations:

$$\frac{\partial \rho}{\partial t} + \nabla \cdot (\rho(u - w)) = 0 \tag{18}$$

$$\frac{\partial \rho u}{\partial t} + \nabla \cdot [\rho u \otimes u - \rho u \otimes w + pI - \sigma] + \rho[\omega \times u] = 0 \tag{19}$$

$$\frac{\partial \rho e_t}{\partial t} + \nabla \cdot [\rho e_t u - \rho e_t w + pu - \sigma \cdot u + k\nabla T] = 0 \tag{20}$$

Note that we have neglected the body forces in this derivation. Inclusion of body forces can be accomplished by setting a nonzero value of C in each case.

e. Flux Vector Form. If we restrict ourselves to just the inviscid portion of the equations, the flux vector form of the governing equations is

$$\frac{\partial \zeta}{\partial t} + \frac{\partial f_i}{\partial x_i} + s = 0 \tag{21}$$

where x_i is the coordinate in the ith direction, and the state and the fluxes for each cell are

$$\zeta = \begin{bmatrix} \rho \\ \rho u_1 \\ \rho u_2 \\ \rho u_3 \\ \rho e_t \end{bmatrix}, \qquad f_i = \begin{bmatrix} \rho u_i - \rho w_i \\ \rho u_i u_1 - \rho w_i u_1 + p\delta_{i1} \\ \rho u_i u_2 - \rho w_i u_2 + p\delta_{i2} \\ \rho u_i u_3 - \rho w_i u_3 + p\delta_{i3} \\ \rho u_i (e_t + p) - \rho w_i e_t \end{bmatrix}$$

$$s = \begin{bmatrix} 0 \\ \rho\omega_2 u_3 - \rho\omega_3 u_2 \\ \rho\omega_3 u_1 - \rho\omega_1 u_3 \\ \rho\omega_1 u_2 - \rho\omega_2 u_1 \\ 0 \end{bmatrix} \tag{22}$$

where $w = w_0 + \Omega \times x$.

This is the formulation implemented in SUmb [26] and used in this work. SUmb is a cell-centered multiblock solver for the Reynolds-averaged Navier–Stokes equations (steady, unsteady, and time-spectral), and it has options for a variety of turbulence models with one, two, and four equations. In this work, we limit ourselves to solving the steady Euler equations.

2. *Constant-Parameter Motions*

Having developed the ability to compute solutions for rotating configurations, we now consider how to compute the required derivatives. To accomplish this, we develop a series of motions that allow for the variation of a single parameter while holding all other parameters constant. Consider pitch rate, q. As described by Limache and Cliff [9], a loop performed at constant α for a given q generates a steady solution. The radius of the loop is inversely proportional to q. Thus, as q reduces to zero, the radius approaches infinity and steady level flight is recovered.

Similar ideas can be applied to roll rate p and yaw rate r. However, in these two other cases, achieving a steady rotating flow is more complicated. When the body axis of the configuration coincides with the wind axis, the logic is the same as for pitching motion. However, if we incline the body axis at an angle of attack, α, relative to the wind, rotation about the body yaw and roll axes no longer yields a

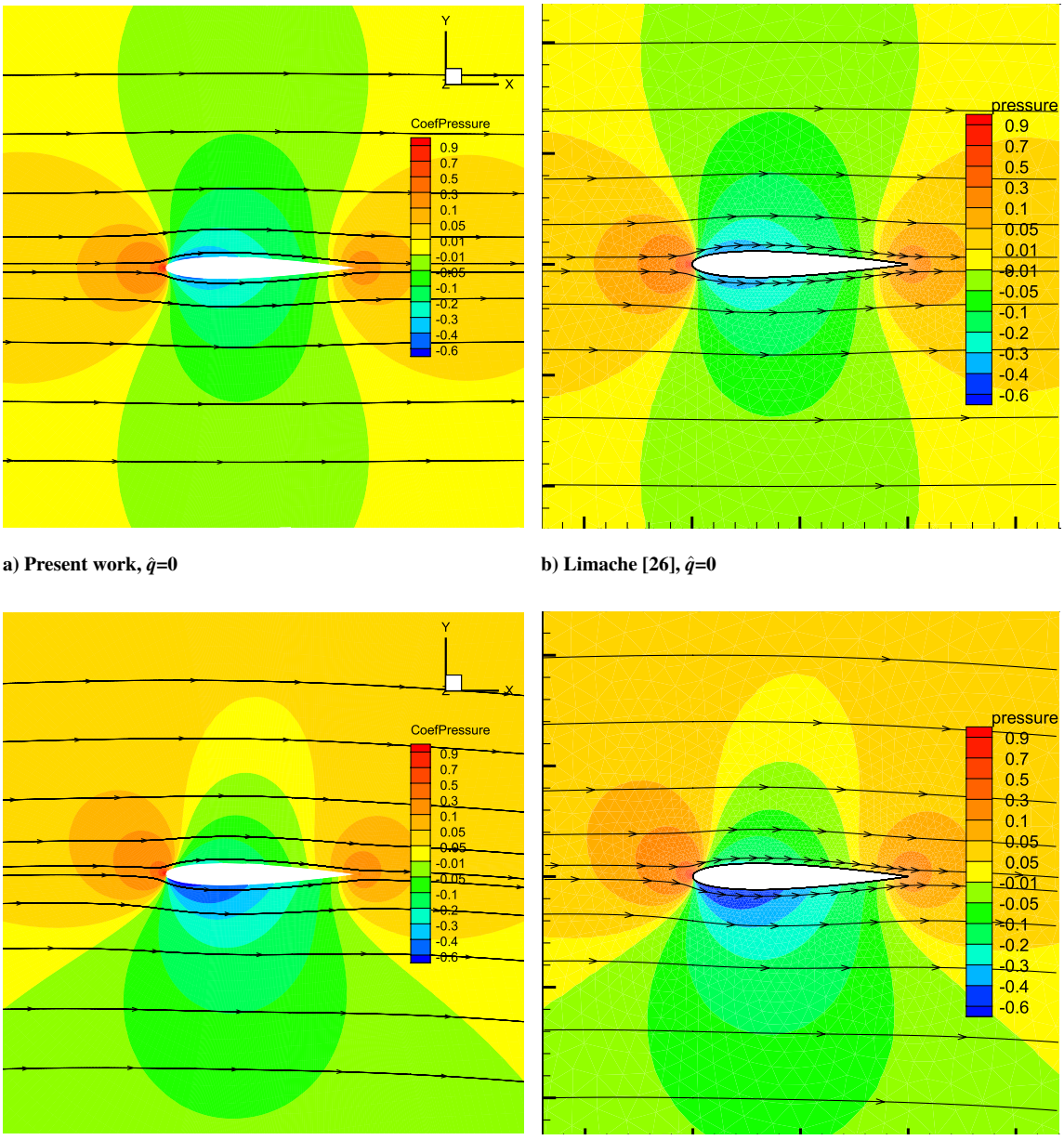

a) Present work, $\hat{q}$=0 **b) Limache [26], $\hat{q}$=0**

c) Present work, $\hat{q}$ =0.01 **d) Limache [26], $\hat{q}$ = 0.01**

Fig. 1 C_p contour and streamline comparison for rotating NACA 0012 at Mach = 0.2, α = 0.

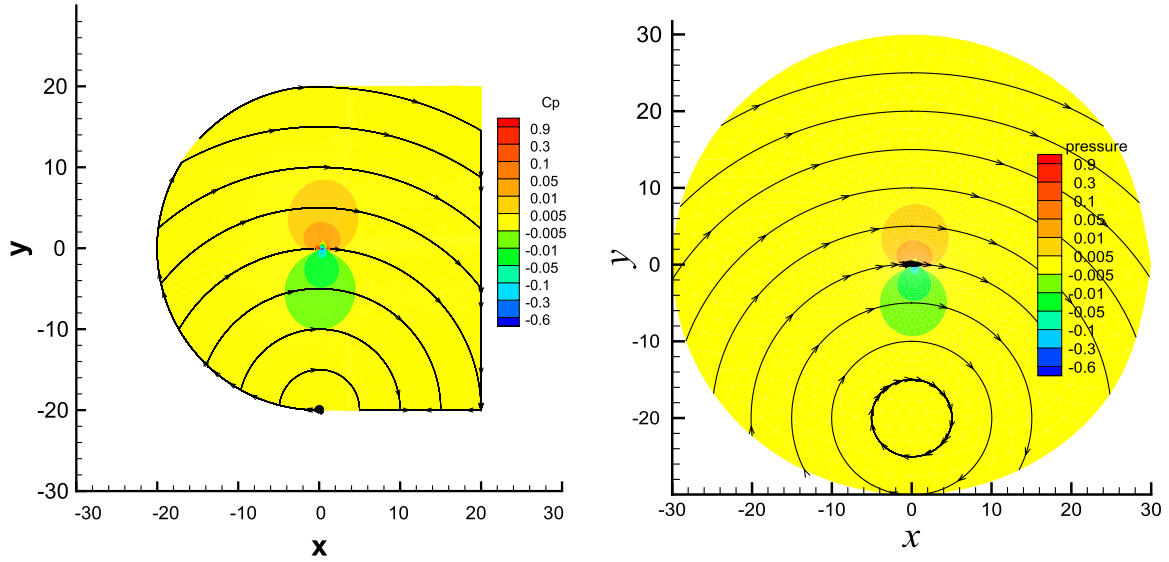

Fig. 2 C_p contour and streamline comparison between present work (left) and Limache [27] (right) for rotating NACA 0012 at Mach $= 0.2$, $\alpha = 0$, and $\hat{q} = 0.05$.

steady-state solution. In this case, rotation about the wind axis is required to generate a steady solution. This requirement is not of great importance for small values of angle of attack, but should be considered for large values.

The results presented in Sec. IV.D show the effect of the two different reference frames. The results presented below are all computed for small angles of attack, so we use the wind-axis reference frame for the computation of the derivatives.

3. *Grid-Motion Considerations*

We selected the moving-grid formulation for this implementation of the stability derivatives, since it was already implemented in SUmb. However, the methods discussed in this paper would apply equally well to a noninertial reference frame formulation. One key observation is that regardless of the chosen formulation, the grid motion must be such that the magnitude of the grid velocity is independent of the rotational rate. More specifically, the grid motion must be specified such that the velocity of the flow at the center of rotation is that of the desired freestream velocity. This condition falls out naturally from the noninertial reference frame formulation, because the velocity is specified in terms of the local grid. For the moving-grid formulation, the correct way to implement this condition is not so obvious. To do so, one needs to specify a grid velocity that is linked to the rotational velocity, such that the velocity of grid's center of rotation is independent of the rotational speed.

B. Verification of Moving-Grid Formulation

To verify the implementation of the moving-grid formulation, we compare results for a NACA 0012 airfoil rotating at a finite $\hat{q}$ to those produced by Limache [27]. In this comparison, we simulate inviscid flow around a NACA 0012 airfoil at Mach $= 0.2$ for $\hat{q} = 0$, 0.01, 0.03, and 0.05.

The C_p distributions around the airfoil are shown in Fig. 1 for both the present and reference results. This figure provides visual verification that the moving-grid formulation implemented in SUmb is consistent with the noninertial reference frame formulation used by Limache [27]. For $\hat{q}$ values of both 0.0 and 0.05, the C_p distributions and streamlines of relative velocity match those presented by Limache.

In Fig. 2 we show the pressure coefficient contours and streamlines of relative velocity in the whole computational domain for $\hat{q} = 0.05$. Note that in both the present work and the reference work, the point of zero relative velocity occurs at the expected coordinates, $(0, -20)$.

Finally, in Table 1 we compare the values of C_l and C_m from our implementation to the references results. The two implementations match very well over a range of $\hat{q}$ values. The largest discrepancy is 0.011 in C_l at Mach $= 0.8$ and $\hat{q} = 0.05$. This close correlation is further confirmation that the formulation is correct.

C. ADjoint Approach

Having modified the CFD code to handle rotating geometries, we can now differentiate the code to obtain stability derivatives. To do this efficiently, we use the ADjoint method, which we have developed in previous work [23]. In this approach, automatic differentiation techniques are combined with the adjoint method to generate the sensitivities for the CFD equations. The application of this method to the computation of stability derivatives is described in this section.

We start by considering the functions of interest, I, which may be either the forces (C_L, C_D, C_Y) or moments (C_l, C_m, C_n) acting on the aircraft. These are functions of both the states of the system (ζ) and the values of the independent variables (x). In this case, the independent variables are the states of the dynamic model $(\alpha, \beta, V, p, q, r, h, \delta_i$, etc.). The function of interest can be expressed as

Table 1 Comparison of lift and moment coefficients for the NACA 0012 at $\alpha = 0$ for various values of $\hat{q}$[a]

Mach	Coefficient	$\hat{q} = 0.00$	$\hat{q} = 0.01$	$\hat{q} = 0.03$	$\hat{q} = 0.05$
0.2	C_l	−0.001 (0.000)	−0.053 (−0.053)	−0.156 (−0.157)	−0.260 (−0.262)
	C_m	0.000 (0.000)	−0.018 (−0.018)	−0.053 (−0.053)	−0.088 (−0.088)
0.5	C_l	0.000 (0.000)	−0.060 (−0.060)	−0.179 (−0.180)	−0.298 (−0.299)
	C_m	0.000 (0.000)	−0.020 (−0.020)	−0.060 (−0.060)	−0.100 (−0.100)
0.8	C_l	0.000 (0.000)	−0.107 (−0.108)	−0.310 (−0.316)	−0.487 (−0.498)
	C_m	0.000 (0.000)	−0.041 (−0.042)	−0.121 (−0.124)	−0.195 (−0.201)

[a]Results from Limache [27] are in parentheses.

Table 2 Verification of derivatives against the complex-step method for NACA 0012 airfoil at Mach = 0.5

Derivative	ADjoint	Complex step
C_{l_α}	7.961756758205	7.961756758114
C_{m_α}	2.068623684859	2.068623684834
C_{l_q}	11.921373826019	11.921373823280
C_{m_q}	−3.999949643166	−3.999949642440

Table 3 ADjoint stability derivatives for a NACA 0012 airfoil at $\alpha = 0.0$ deg

Mach	Derivative	ADjoint	Limache and Cliff. [9]	% Difference
0.1	C_{l_q}	10.385	10.377	0.08%
0.1	C_{m_q}	−3.498	−3.489	0.26%
0.5	C_{l_q}	11.921	11.847	0.62%
0.5	C_{m_q}	−4.000	−3.968	0.81%
0.8	C_{l_q}	21.782	21.889	0.49%
0.8	C_{m_q}	−8.438	−8.884	5.02%

Table 4 ONERA M6 geometry parameters

Parameter	Value
Half-span, m	1.1963
Half-wing area, m^2	0.753
Leading-edge sweep, deg	30
Taper	0.562
Twist, deg	0
Airfoil	ONERA D, normal to 40% chord line

$$I = I(x, \zeta(x)) \tag{23}$$

We can also represent the solution of the CFD equations as a set of governing equations that are functions of the states and the independent variables. The residuals of these equations can be written as

$$\mathcal{R}(x, \zeta(x)) = 0 \tag{24}$$

To derive the adjoint equations for this system, we first write the total derivative for both the function of interest (23) and the residuals (24), which yields

$$\frac{\mathrm{d}I}{\mathrm{d}x} = \frac{\partial I}{\partial x} + \frac{\partial I}{\partial \zeta}\frac{\mathrm{d}\zeta}{\mathrm{d}x} \tag{25}$$

and

$$\frac{\mathrm{d}\mathcal{R}}{\mathrm{d}x} = \frac{\partial \mathcal{R}}{\partial x} + \frac{\partial \mathcal{R}}{\partial \zeta}\frac{\mathrm{d}\zeta}{\mathrm{d}x} = 0 \tag{26}$$

because $\mathcal{R} = 0$, regardless of x, when the governing equations are satisfied. Therefore, we can rewrite the total derivative from Eq. (26) as

$$\frac{\mathrm{d}\zeta}{\mathrm{d}x} = -\left[\frac{\partial \mathcal{R}}{\partial \zeta}\right]^{-1}\frac{\partial \mathcal{R}}{\partial x} \tag{27}$$

Combining Eqs. (25) and (27), we obtain

$$\frac{\mathrm{d}I}{\mathrm{d}x} = \frac{\partial I}{\partial x} - \frac{\partial I}{\partial \zeta}\left[\frac{\partial \mathcal{R}}{\partial \zeta}\right]^{-1}\frac{\partial \mathcal{R}}{\partial x} \tag{28}$$

We now have the total derivative $\mathrm{d}I/\mathrm{d}x$ expressed in terms of four partial derivatives that do not require a solution of the residual equations in their computation. Instead, to compute the total derivative $\mathrm{d}I/\mathrm{d}x$, we must perform a series of linear solutions. In our case, we solve the adjoint system,

$$\left[\frac{\partial \mathcal{R}}{\partial \zeta}\right]^T \Psi = -\frac{\partial I}{\partial \zeta} \tag{29}$$

which requires a separate linear solution for each component of I. The other option, the direct method, involves solving

$$\left[\frac{\partial \mathcal{R}}{\partial \zeta}\right]\frac{\mathrm{d}\zeta}{\mathrm{d}x} = -\frac{\partial \mathcal{R}}{\partial x} \tag{30}$$

which requires a separate linear solution for each component of x. The relative efficiency of the two approaches depends on the relative sizes of I and x. In this case, the size of I is six and the size of x is six or more, depending on the number of control derivatives required. Therefore, it is slightly more favorable to use the adjoint method, but the relative numbers are close enough that there is no significant advantage. In our case, the adjoint approach is used because it has

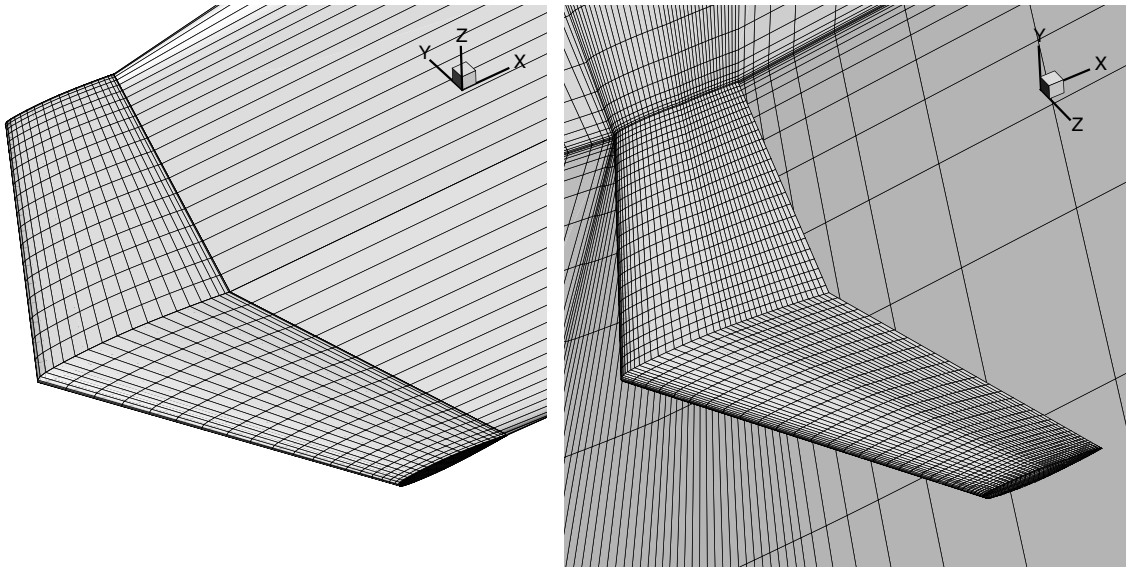

a) PMARC **b) SUmb**

Fig. 3 Meshes for the ONERA M6 case.

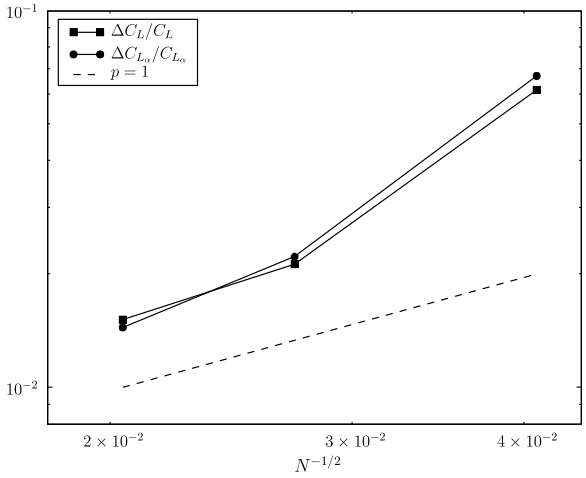

Fig. 4 PMARC mesh convergence study, Mach = 0.1 and $\alpha = 3$ deg.

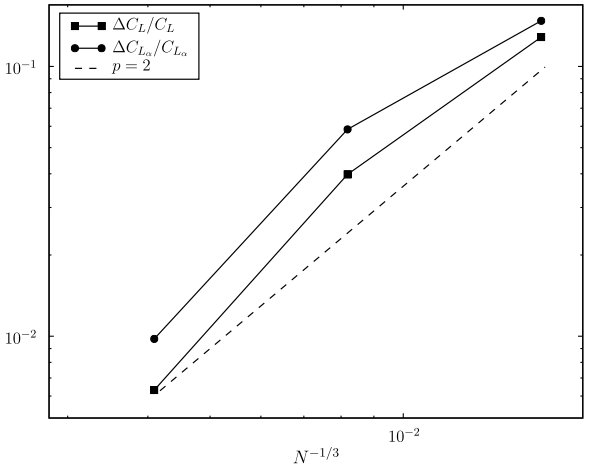

Fig. 5 SUmb mesh convergence study, Mach = 0.8395 and α= 3.06 deg.

already been implemented to compute the derivatives for design optimization [28]. In design optimization, the number of design variables generally exceeds the number of functions of interest, and the adjoint approach is decidedly advantageous.

The other consideration associated with Eq. (28) is how to calculate the four partial derivatives that make up the expression. This is where automatic differentiation is used. One of the most significant drawbacks of the adjoint method outlined above is that the calculation of the partial derivatives making up the expression can be extremely complex. In many cases, such as those involved in complex CFD schemes, the effort required to differentiate the code used to compute the residuals is tremendous. By using automatic differentiation to compute these derivatives, the amount of effort required to complete the differentiation is significantly reduced. In addition, no approximations are made in the differentiation, and as a result, the derivatives computed with the ADjoint method are extremely accurate.

D. Verification of the ADjoint for Stability Derivatives

To verify the ADjoint implementation for the computation of stability derivatives, we reproduce the NACA 0012 airfoil case of Limache and Cliff [9]. We use a pseudo-two-dimensional mesh, which is two cells in the spanwise direction, with symmetry planes at the ends of the wing segment to reproduce two-dimensional flow. Each slice of the mesh contains 65,536 cells for a total mesh size of 131,072 cells. The flow is simulated at $\alpha = 0$ and Mach = 0.1, 0.5 and 0.8, with the flow solutions converged to a relative convergence tolerance of 10^{-12}. We make two comparisons: one to verify consistency within our implementation, and another to verify our results against those of Limache and Cliff.

To verify the consistency within our implementation, we compare the ADjoint derivatives against derivatives computed using the complex-step derivative approximation [29]. The purpose of this verification is to show that the ADjoint implementation accurately computes the derivative of the code in the SUmb solver. Using the complex-step approach, the derivatives are computed by

$$\frac{\mathrm{d}I(x)}{\mathrm{d}x} = \frac{\mathrm{Im}[I(x+ih)]}{h} + \mathcal{O}(h^2) \tag{31}$$

where $i = \sqrt{-1}$. This approximation is not subject to the subtractive cancellation errors inherent in finite differences. Therefore, with a sufficiently small step size (in this case, 10^{-20}), the method is able to produce derivatives with the same accuracy as the flow solution, making it a solid benchmark for our results.

The ADjoint derivatives are compared with the complex-step results in Table 2, where we can see that the results match by 9 to 11 digits. This is an extremely accurate match, far beyond the accuracy of the underlying physical model used. Furthermore, given the iterative nature of the solvers used, the accuracy is consistent with the 10^{-12} relative convergence tolerance that was achieved.

The verification against the results of Limache and Cliff [9] is shown in Table 3. This comparison is done to show that our method accurately captures the dependencies of the coefficients on q. As can be seen in Table 3, the code from this work is accurate relative to the

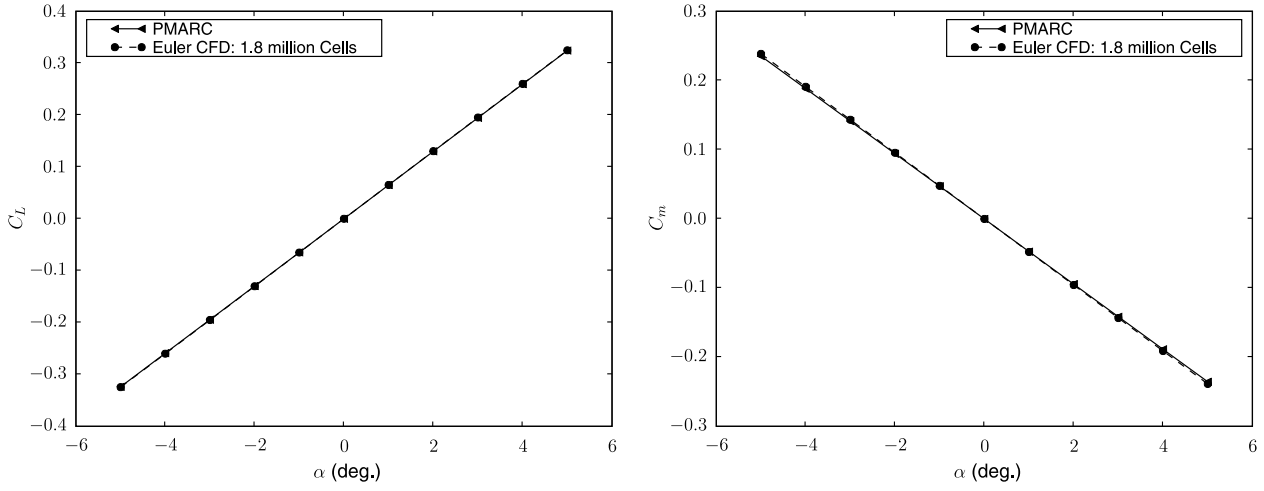

Fig. 6 ONERA M6: Coefficients vs α, Mach = 0.1 and $x_{\mathrm{ref}} = 0$.

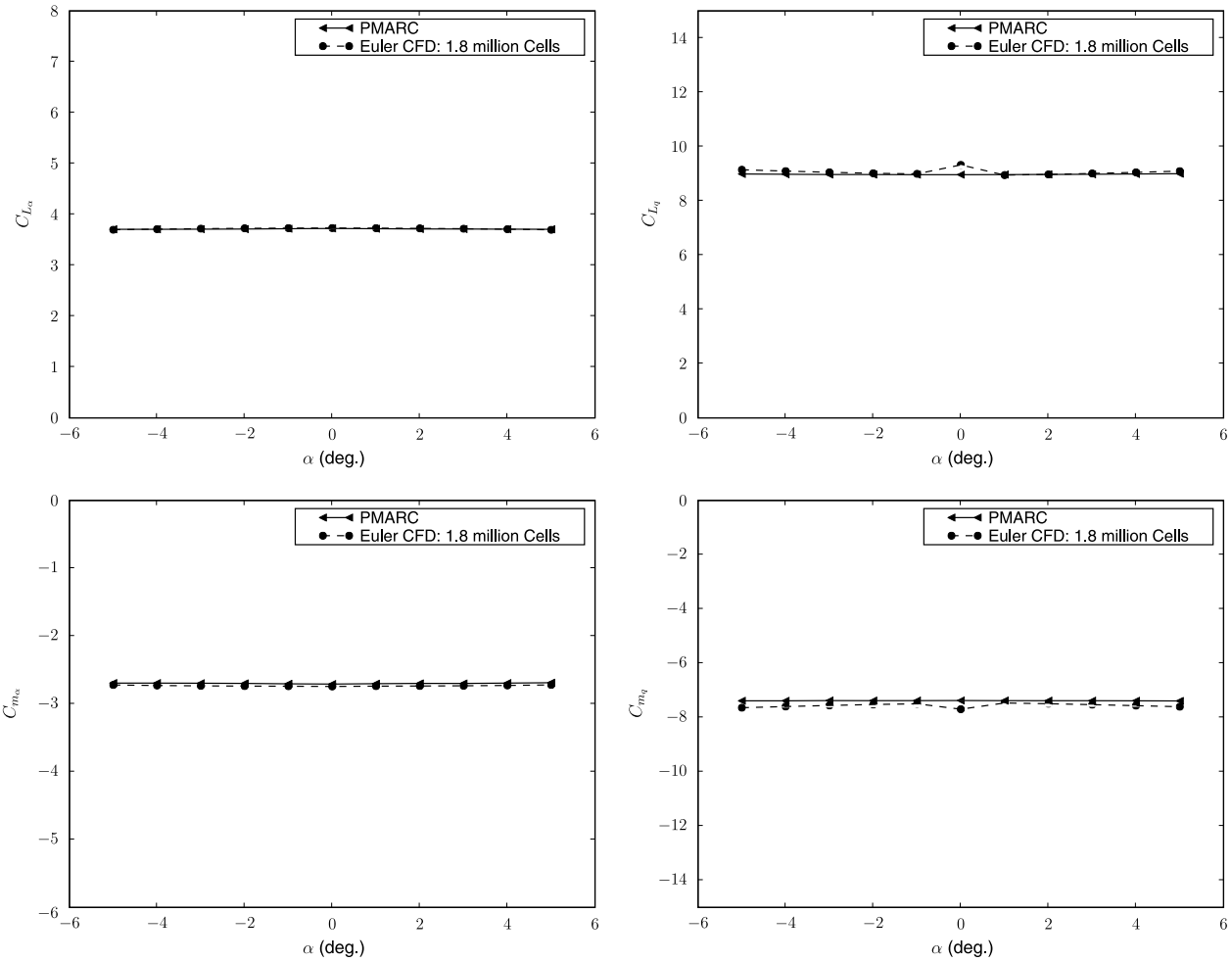

Fig. 7 ONERA M6: longitudinal derivatives vs α, Mach $= 0.1$ and $x_{\text{ref}} = 0$.

reference implementation of Limache and Cliff [9]. For the Mach $=$ 0.1 and 0.5 cases, the differences relative to the reference results are less than 1%. In the Mach $= 0.8$ case, C_{l_q} is within 1% of the reference results, while C_{m_q} differs by approximately 5%. This larger discrepancy can be attributed to the fact that there is a shock wave in the solution for Mach $= 0.8$. The precise location of the shock has a significant impact on the value of the moment coefficient and hence on the moment coefficient derivatives as well. Given that SUmb is a structured multiblock code and that the reference results were computed with an unstructured code, slight variations in the prediction of the shock location are expected. Based on these results, we conclude that the stability derivatives predicted by the code are correct for the NACA 0012 airfoil case.

IV. ONERA M6 Stability Derivatives

To verify the derivative computation in three dimensions, we analyze the ONERA M6 wing, which is a common test case in the CFD community [30]. The configuration is a simple swept wing; the geometry parameters for the wing are listed in Table 4.

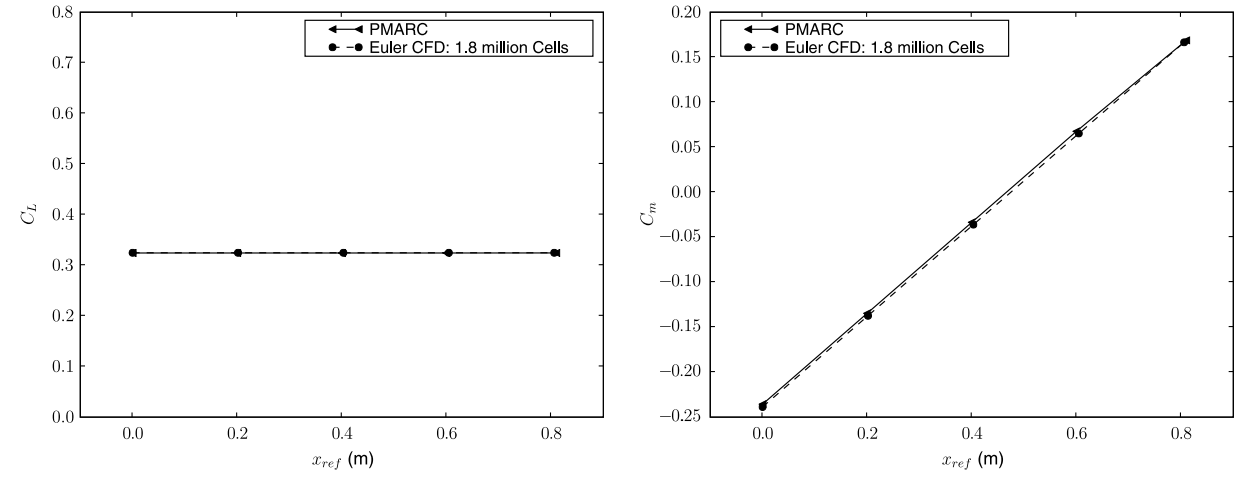

Fig. 8 ONERA M6: Coefficients vs x_{ref}, Mach $= 0.1$ and $\alpha = 5$ deg.

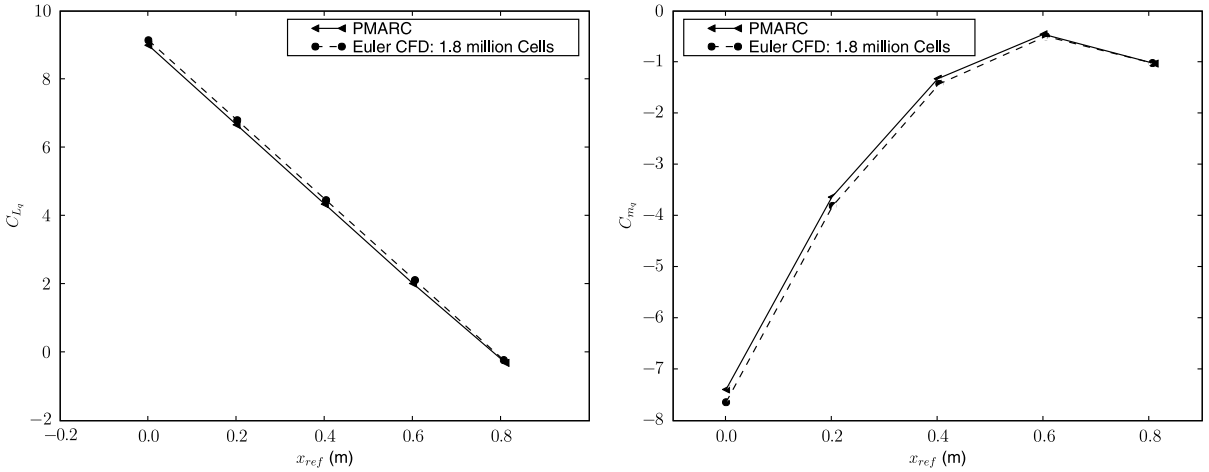

Fig. 9 ONERA M6: longitudinal derivatives vs x_{ref}, Mach = 0.1 and $\alpha = 5$ deg.

In this study, we compare the derivatives for the ONERA M6 wing at Mach = 0.1 against those calculated with PMARC, a well-established panel code used for low-speed flow prediction [31]. The comparisons show the values of various coefficients and derivatives for a variety of flight conditions (i.e., various values of α and β) and rotational center locations (x_{ref}). The purpose of these comparisons is to show that the proposed method accurately captures the various dependencies in the stability derivative computation.

Finally, we present derivative values for the ONERA M6 wing at Mach = 0.8395 and $\alpha = 3.06$ deg, one of the flight conditions tested by AGARD [30]. These transonic derivatives are intended to become reference values for future work. Note that the rotational derivatives are expressed in terms of normalized rotational rates $\hat{p}$, $\hat{q}$, and $\hat{r}$. The derivatives are expressed in a typical body-axis reference frame with the x axis pointing forward and the z axis pointing down. SUmb computations are conducted in a reference frame with the x

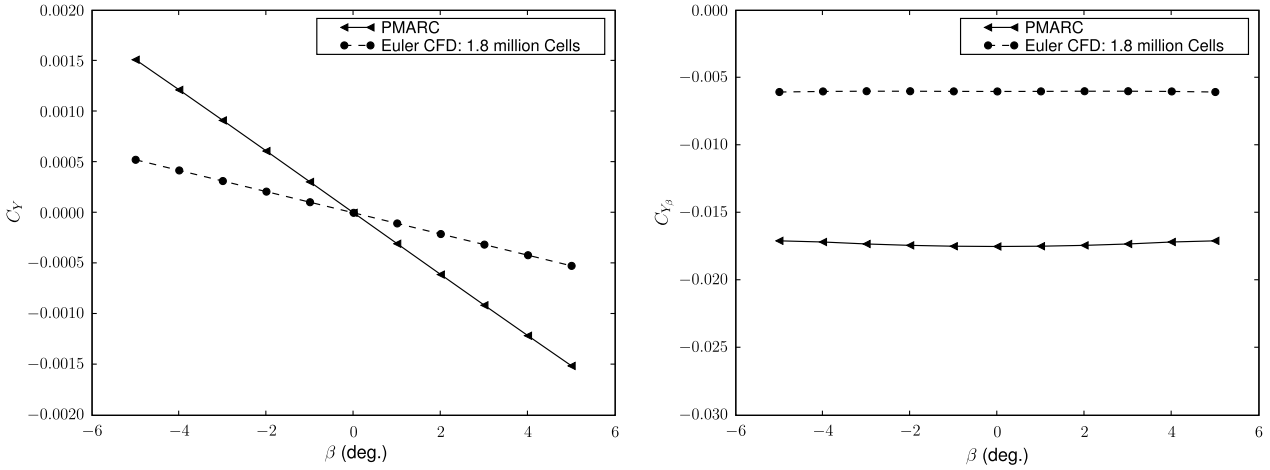

a) C_Y vs. β, Mach = 0.1, α= 5 deg

b) $C_{Y\beta}$ vs. β, Mach =, 0.1, β = 0.0

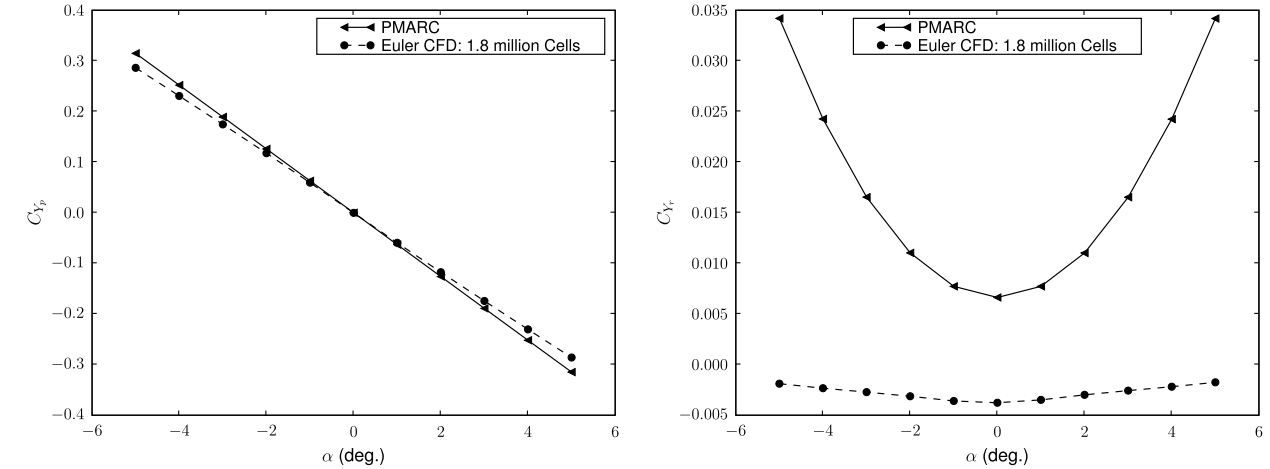

c) C_{Yp} vs. α, Mach = 0.1, β = 0.0

d) C_{Y_r} vs. α, Mach =, 0.1, β = 0.0

Fig. 10 ONERA M6: C_Y and derivatives.

axis pointing in the downstream direction and the z axis pointing out toward the left half of the wing.

A. Mesh Convergence

To verify the stability derivative formulation discussed in the present work, solutions from PMARC are compared against solutions from SUmb.

The PMARC mesh is shown in Fig. 3a. Each wing half is composed of three patches: one that wraps around the leading edge forming the wing surface, another for the wing tip, and a third one for the wake, which is attached to the trailing edge. The wake patch is rigid and aligned with the freestream direction.

To demonstrate the numerical accuracy of the PMARC solutions, a convergence study was performed by increasing the number of cells per side in each patch from 5 to 20 in increments of 5. The wake patches and wing tip patches have the same number of cells in each direction, while the main wing patches have twice as many cells in the chordwise direction as in the spanwise direction. The convergence of the C_L and C_{L_α} values for this series of meshes is shown in Fig. 4. This plot shows that C_L and C_{L_α} converge as the meshes are refined. For the PMARC results, the error between the two finest meshes is 1.5% for C_L and 1.6% for C_{L_α}.

A sample of the SUmb mesh is shown in Fig. 3b. It is an H-H mesh for which the wing tip is closed with a rounded tip, and the trailing edge of the wing has zero thickness. The far-field boundary is approximately 30 mean aerodynamic chords away from the wing. To quantify the numerical accuracy of the solution, a series of four meshes have been generated. Each mesh is exactly 8 times larger than the previous mesh, which is the result of doubling the mesh points for each edge. The meshes have a total of 28,000, 228,000, 1.8 million, and 14.7 million cells, respectively. The offwall spacing for the 14.7-million-cell mesh is 1×10^{-3} m. The leading-edge spacing is also 1×10^{-3} m and the trailing-edge spacing is 5×10^{-3} m. The mesh shown in Fig. 3b is the 228,000 cell mesh. C_L and C_{L_α} convergence results for this series of meshes are shown in Fig. 5. These plots show that the difference between the finest two meshes is 0.7% for C_L and 1.1% for C_{L_α}. The fact that the error for the PMARC results is on the order of 2% and the error for the SUmb results is on the order of 1% gives confidence in the quality of the results presented. The plots shown in Secs. IV.B–IV.D are generated using the 20-cell-per-side PMARC meshes and the 1.8-million-cell SUmb mesh. The benchmark derivative results presented in Sec. IV.E are calculated with the 14.7-million-cell SUmb mesh.

B. Low-Speed Verification: Longitudinal Derivatives

The first verification we show is the variation of the longitudinal coefficients (C_L, C_m) and their derivatives with respect to α. Figure 6 shows the variation the coefficients and Fig. 7 shows the variation of the various derivatives, both with respect to α. We then compare the performance of these same coefficients and derivatives for a variety of longitudinal reference points, x_{ref}. This reference point location acts as both the center of moment and the center of rotation. Figure 8 shows the variation of the coefficients with respect to x_{ref} and Fig. 9 shows the variation of the derivatives with respect to the same point.

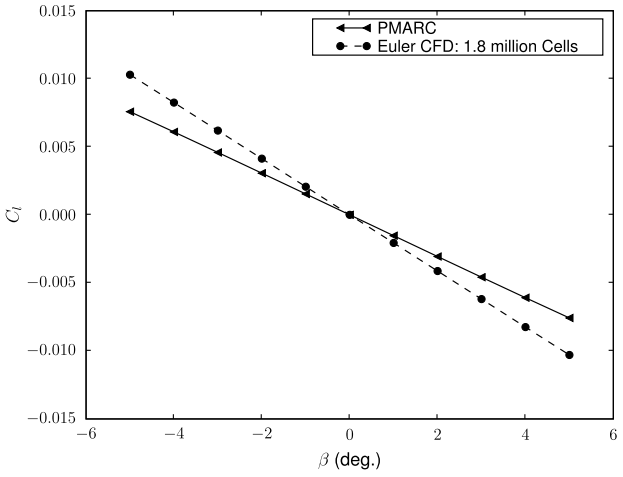

a) C_l vs. β, Mach = 0.1, α = 5.0 deg

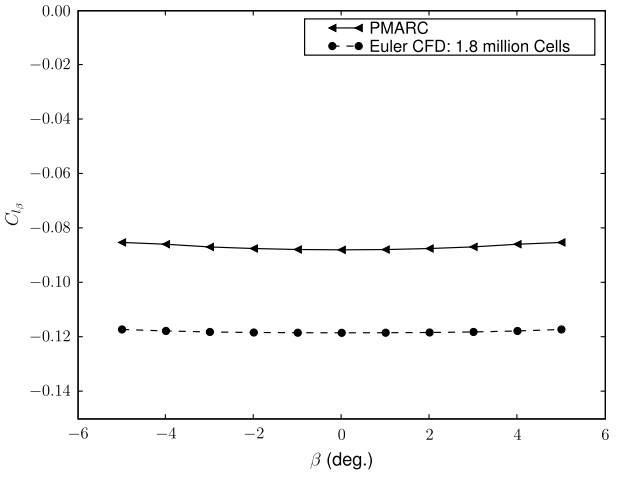

b) C_{l_β} vs. β, Mach = 0.1, α = 5.0 deg

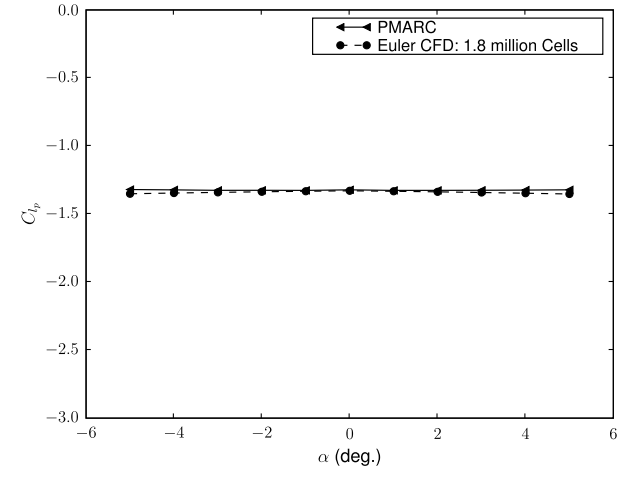

c) C_{l_p} vs. α, Mach = 0.1, β = 0.0

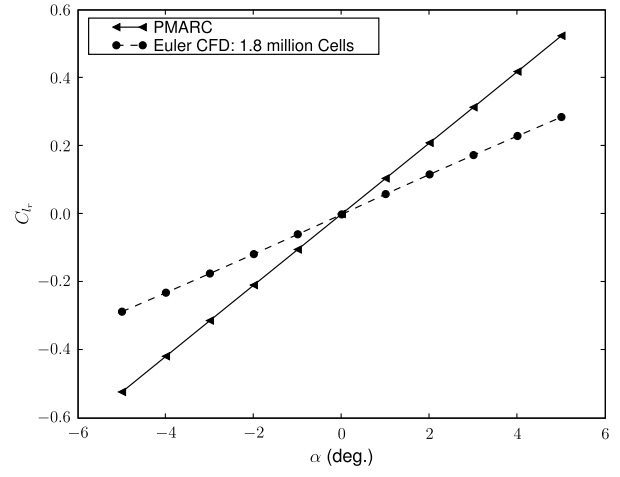

d) C_{l_r} vs. α, Mach = 0.1, β = 0.0

Fig. 11 ONERA M6: C_l and derivatives.

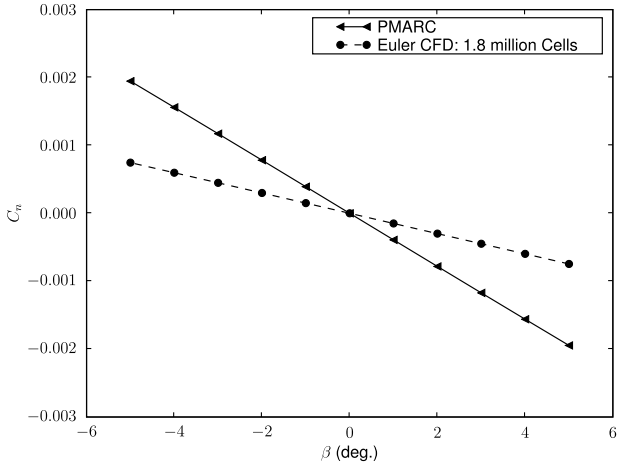

a) C_n vs. β, Mach = 0.1, α = 5.0

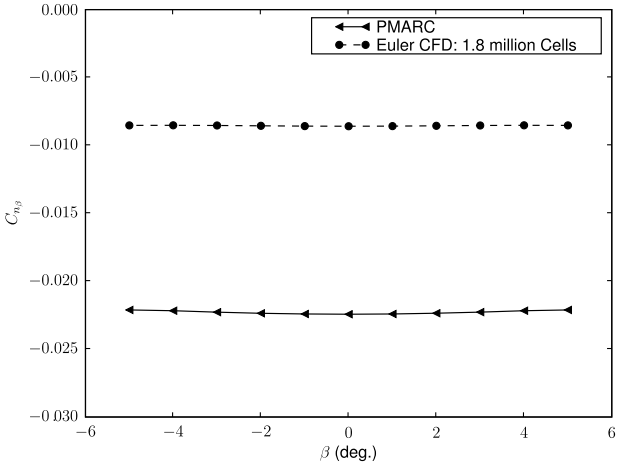

b) C_{n_β} vs. β, Mach = 0.1, α = 5.0

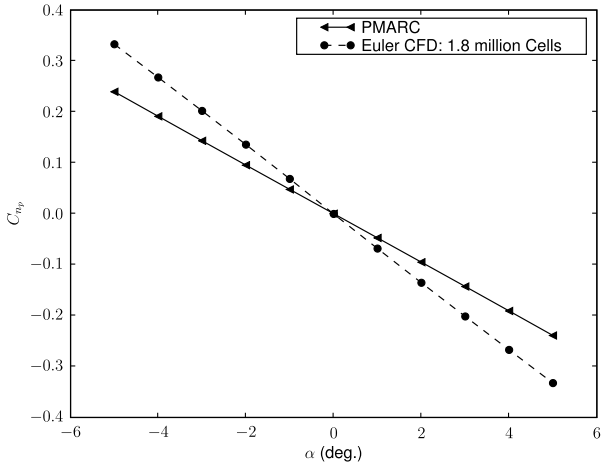

c) C_{n_p} vs. α, Mach = 0.1, β = 0.0

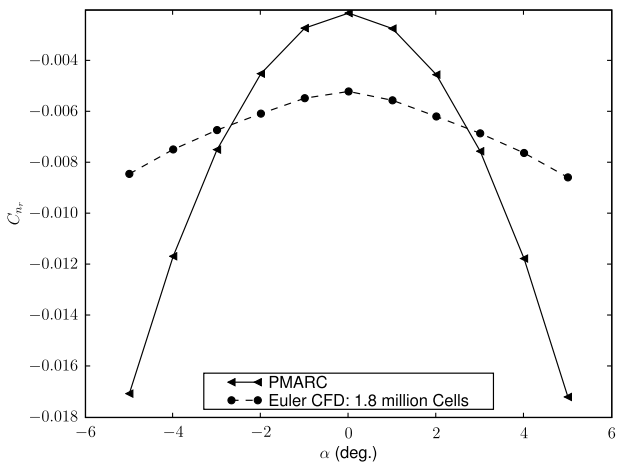

d) C_{n_r} vs. α, Mach = 0.1, β = 0.0

Fig. 12 ONERA M6: C_n and derivatives.

As we can see from these figures, the longitudinal characteristics of the wing are well captured by our computations. There is essentially no variation between the slopes predicted by SUmb and PMARC for the coefficients shown in Figs. 6a and 6b. The comparisons in Fig. 7 show consistent performance over the full range of α's tested. The derivative values predicted by PMARC and SUmb are slightly different, but the trends for both methods match, leading to a consistent difference between the two values. We see similar trends over the range of x_{ref} values considered in Figs. 8 and 9. In each case, the trend of the PMARC results closely matches the trend in the SUmb result. This even holds for the more complex curved trend shown in Fig. 9b.

From all these comparisons, we conclude that the longitudinal stability derivatives computed by SUmb are correct, as long as the physics captured by the Euler equations accurately model the problem of interest.

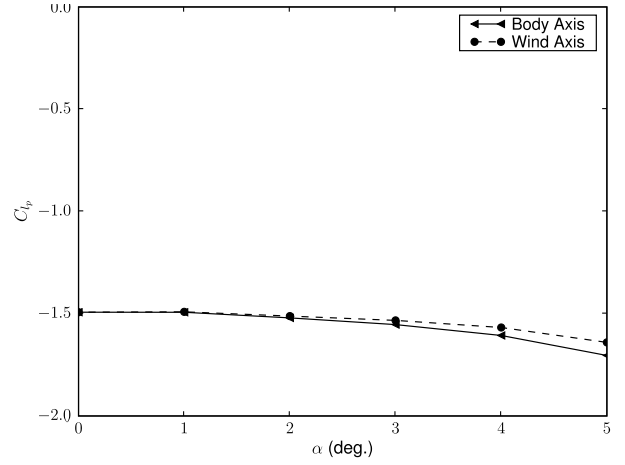

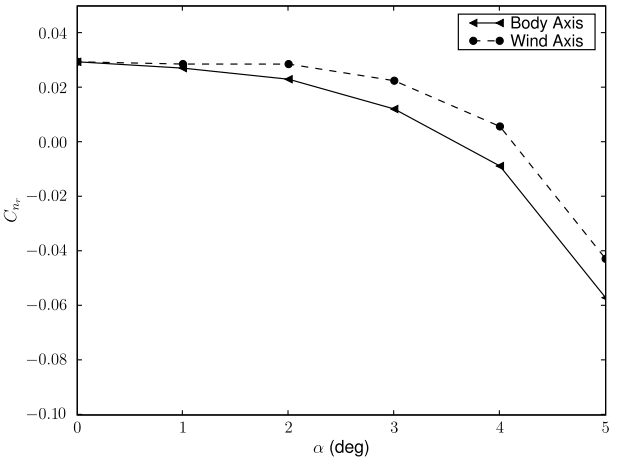

Fig. 13 ONERA M6: Comparison of wind-axis versus body-axis computations.

Table 5 Comparison for C_{l_p} for wind-axis and body-axis computations

α	Wind	Body	Error	% error
0	−1.4926016	−1.4926016	0.0000	0.00%
1	−1.4908012	−1.4929310	0.0021	−0.14%
2	−1.5116103	−1.5204085	0.0088	−0.58%
3	−1.5326331	−1.5531822	0.0205	−1.32%
4	−1.5674002	−1.6063816	0.0390	−2.43%
5	−1.6402228	−1.7041819	0.0640	−3.75%

Table 6 Comparison of C_{n_r} for wind-axis and body-axis computations

α	Wind	Body	Error	% error
0	2.9516551×10^{-2}	2.9516551×10^{-2}	0.0000	0.00%
1	2.8696904×10^{-2}	2.7199394×10^{-2}	0.0015	5.51%
2	2.8677435×10^{-2}	2.3128088×10^{-2}	0.0055	23.99%
3	2.2586010×10^{-2}	1.2211285×10^{-2}	0.0104	84.96%
4	5.8047916×10^{-3}	$-8.7061377 \times 10^{-3}$	0.0145	−166.67%
5	$-4.2725415 \times 10^{-2}$	$-5.6996461 \times 10^{-2}$	0.0143	−25.04%

C. Low-Speed Verification: Lateral Derivatives

Next, we examine the lateral coefficients (C_Y, C_l, C_n) and their derivatives. The lateral coefficients are all zero for the symmetric flight condition at $\beta = 0$, and therefore we show the variation of these coefficients for a variety of sideslip angles β. The variations for C_Y, C_l, and C_n are plotted in Figs. 10a, 11a, and 12a, respectively.

While the values of the coefficients themselves are zero at the symmetric flight condition, the values of their derivatives are not. Therefore, to evaluate the derivatives of the lateral coefficients, we examine the derivatives for a range of α values. In this section, the figures are split into groups by coefficient. Each group shows the variation of the coefficient for a variety of values of β at $\alpha =$ 5 degrees, as well as the variation of the coefficient derivatives with respect to β, p, and r for a range of α values. Figure 10 shows the values for C_Y, Fig. 11 shows the values for C_l, and Fig. 12 shows the values for C_n.

The variation in the slopes between the SUmb computed coefficients and the PMARC computed coefficients is larger for the lateral derivatives than for the longitudinal derivatives. However, the dominant trends are the same for both sets of results. C_{Y_β} is essentially constant with β for both cases. C_{Y_p} decreases with α, and C_{Y_r} has a nonlinear dependence on α. Similar trends are exhibited by the C_l derivatives. C_{l_β} is constant with β, C_{l_p} is constant with α, and C_{l_r} increases with increasing α. Finally, for the C_n derivatives, we see that for both cases C_{n_β} is essentially constant with β, C_{n_p} decreases with α, and C_{n_r} has a curved shape.

In this particular case, the discrepancies between the PMARC derivatives and the SUmb derivatives are largest for the C_n and C_Y derivatives. This is due to the fact that both the coefficients and the derivatives are very small, on the order of 10^{-3}, making it difficult to compute them accurately. Furthermore, the lateral forces are more difficult to predict due to the fact that the ONERA M6 wing has no dihedral. In this case, the lateral forces in inviscid flow are dominated by the flow at the wing tips, which is complicated in asymmetric flow. However, as noted above, even though there are differences in the value predicted by the methods, the trends in the two methods match, indicating that the formulation is capturing the necessary dependencies.

D. Wind-Axis Versus Body-Axis Derivatives

As mentioned in Sec. III.A.2, it is not possible to physically isolate the lateral body-axis derivatives of the aircraft for nonzero angles of attack. However, because the ADjoint method calculates the derivatives from a single reference flow solution, we are able to compute derivatives about either the wind axis or the body axis at that reference solution. As long as the computation of the reference solution is possible, the ADjoint approach can linearize about that point, even if the lateral rotation about the body axis would not yield a steady flow solution.

In this section, we compare the wind-axis derivatives to the body-axis derivatives. From this comparison, we can assess the validity of using wind-axis derivatives in place of body-axis derivatives for small angles of attack. In Figs. 13a and 13b, we plot the variation of C_{l_p} and C_{n_r} versus α for both the wind-axis case and the body-axis case. Tables 5 and 6 show the values of the same two derivatives for α values from 0 to 5 deg for both the body- and wind-axis derivatives at Mach = 0.8395.

From these results, we can see a clear divergence of the two predicted values as the value of α increases. However, for the low values of α seen here, the variation is relatively small, staying under 5% for the C_{l_p} derivatives. Based on these results, we conclude that the values of the wind-axis derivatives are accurate enough to be useful. However, for larger angles of attack, a correction would likely be needed to produce useful results.

E. High-Speed Derivative Values

To provide a benchmark for future work, we compute the values of the wind-axis and body-axis stability derivatives for a transonic flight condition. Figures 14a and 14b show the chordwise pressure profiles for the 20 and 90% span positions on the wing, both from experimental data [30] and from the 14.7-million-cell mesh used in

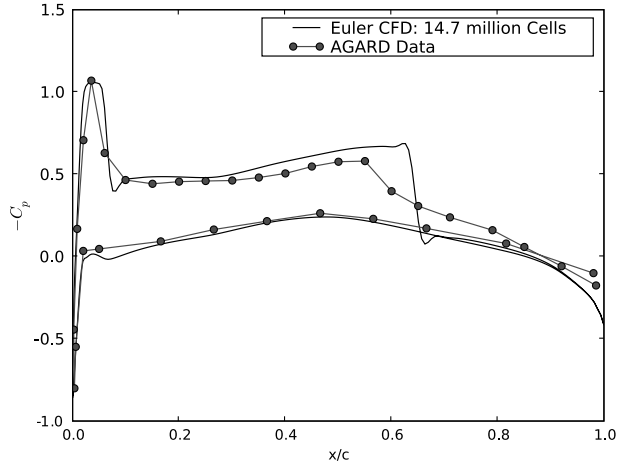

a) Chordwise C_p distribution at 20% span

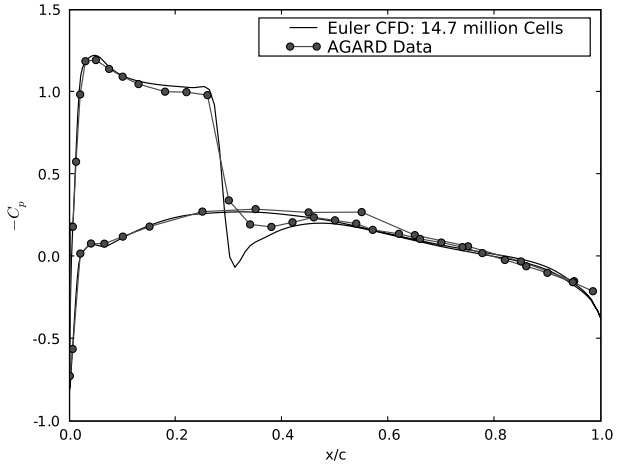

b) Chordwise C_p distribution at 90% span

Fig. 14 ONERA M6: Mach = 0.8395 test case validation.

Table 7 Body-axis derivatives at Mach = 0.8395, $\alpha = 3.06$, and $x_{\text{ref}} = 0.0$ m

Parameter	C_L	C_D	C_Y	C_l	C_m	C_n
α	5.5772	4.5422×10^{-01}	~ 0	~ 0	-4.0932	~ 0
β	-1.5168×10^{-05}	4.0961×10^{-06}	-6.8243×10^{-03}	-1.2667×10^{-01}	1.4722×10^{-05}	1.4088×10^{-02}
Mach	7.7872×10^{-01}	1.3225×10^{-01}	~ 0	~ 0	-8.3126×10^{-01}	~ 0
$\hat{p}$	-2.3528×10^{-06}	3.5867×10^{-07}	2.4044×10^{-01}	-1.5185	2.2824×10^{-06}	-2.1186×10^{-01}
$\hat{q}$	1.3474×10^{01}	6.0271×10^{-01}	~ 0	~ 0	-1.1437×10^{01}	~ 0
$\hat{r}$	1.3981×10^{-06}	-4.2876×10^{-07}	-3.3960×10^{-02}	3.6030×10^{-01}	-1.3639×10^{-06}	1.2700×10^{-02}

Table 8 Wind-axis derivatives at Mach = 0.8395, $\alpha = 3.06$, and $x_{\text{ref}} = 0.00$ m

Parameter	C_L	C_D	C_Y	C_l	C_m	C_n
α	5.5772	4.5422×10^{-01}	~ 0	~ 0	-4.0932	~ 0
β	-1.5168×10^{-05}	4.0961×10^{-06}	-6.8243×10^{-03}	-1.2667×10^{-01}	1.4722×10^{-05}	1.4088×10^{-02}
Mach	7.7872×10^{-01}	1.3225×10^{-01}	~ 0	~ 0	-8.3126×10^{-01}	~ 0
$\hat{p}$	-2.2748×10^{-06}	3.3527×10^{-07}	2.3829×10^{-01}	-1.4971	2.2063×10^{-06}	-2.1088×10^{-01}
$\hat{q}$	1.3474×10^{01}	6.0271×10^{-01}	~ 0	~ 0	-1.1437×10^{01}	~ 0
$\hat{r}$	1.5217×10^{-06}	-4.4730×10^{-07}	-4.6747×10^{-02}	4.4085×10^{-01}	-1.4838×10^{-06}	2.3991×10^{-02}

Table 9 ADjoint timing for the ONERA M6 case at Mach = 0.8395 and $\alpha = 3.06$ deg[a]

	C_L	C_D	C_Y	C_l	C_m	C_n	Total time
Number of processors				32			
Flow solution	267	——	——	——	——	——	267
ADjoint solution	466	279	272	258	276	308	1859
Breakdown:							
Computation of residual matrices	117	——	——	——	——	——	117
Computation of preconditioning matrix	26	——	——	——	——	——	26
Computation of right-hand side	1	1	1	1	1	1	6
Solution of the adjoint equations	321	277	270	256	274	306	1704
Computation of the total sensitivities	1	1	1	1	1	1	6

[a]With ~ 1.8 million cells and 10^{-10} relative convergence; all times are in seconds.

this study. While there are slight errors in the predicted location of the shock wave in the solution, on the whole, the solutions match well. This comparison shows that the Euler model used in this work is representative of the flow in this case. Furthermore, based on the comparisons shown in the previous section, we conclude that the stability derivative formulation presented in this work is correct and applicable to any flows for which the flow solver produces valid results.

The body-axis derivatives for the transonic test case are listed in Table 7, and the wind-axis derivatives for the same case are listed in Table 8.

V. Computational Performance

In addition to demonstrating the accuracy of the code, it is important to show its computational efficiency. To this end, we examined the time required to compute the various derivatives required in the generation of a simple linear flight dynamic model. The results in Table 9 show the computational time needed to evaluate the six consecutive adjoint problems (C_L, C_D, C_Y, C_l, C_m, and C_n) required to generate all of the static and dynamic derivatives for a given configuration. The linear system solutions required for the adjoint system are computed using the PETSc package[‡] developed at Argonne National Labs [32]. This is a broadly applicable scientific computing package that contains a variety of linear and nonlinear solution methods, as well as a variety of preconditioning options. In this work, we are using the restarted GMRES solver with an additive Schwartz parallel preconditioner. Local preconditioning is accomplished with incomplete lower/upper factorization and a reverse Cuthill–McKee reordering. The computations for this work were performed on the SciNet general-purpose cluster, which uses 2.5 GHz Intel Nehalem Processors with eight cores and 16 GB RAM per node. The timings shown in Table 9 are run on four nodes connected by Infiniband for a total of 32 processors.

As we see from the table, the flow solution takes approximately 5 min, while a single ADjoint solution takes only 8 min. The total time for computing all six ADjoint solutions required to evaluate the necessary stability derivatives is only 31 min. At this level of efficiency, the computational cost of computing the derivatives is low enough to be used for design.

VI. Conclusions

In this paper, a method for the computation of static and dynamic stability derivatives of arbitrary configurations was presented. The method combines the ADjoint sensitivity analysis technique with a moving-grid CFD solver to allow for the efficient computation of static and dynamic derivatives. For the longitudinal derivatives, the method was shown to match existing methods to within 1% for subsonic cases and to within 1–5% for transonic cases.

For a more general three-dimensional case, the method compared well with an existing panel code method, PMARC. Both lateral and longitudinal derivatives were examined at Mach = 0.1 and the results showed similar trends for both methods.

Finally, the cost of computing a full set of stability derivatives using this new method was measured. For a 1.8-million-cell case, the flow solution and the six ADjoint solutions required about 30 min on 32 processors (2.5 GHz Intel Nehalem). At this level of computational cost, it is certainly possible to consider using stability derivative data in the design process.

Acknowledgments

The authors are grateful for the funding provided by the Canada Research Chairs program and the Natural Sciences and Engineering

[‡]Data available online at http://www.mcs.anl.gov/petsc [retrieved 24 June 2011].

Research Council. Computations were performed on the general-purpose cluster supercomputer at the SciNet high-performance computing consortium, which is funded by the Canada Foundation for Innovation under the auspices of Compute Canada, the Government of Ontario, Ontario Research Fund—Research Excellence, and the University of Toronto. The authors would also like to thank Edwin van der Weide and Juan J. Alonso for their assistance in the early stages of this project and, in particular, with the moving-grid formulation in the SUmb flow solver.

References

[1] Etkin, B., *Dynamics of Atmospheric Flight*, Dover, Mineola, NY, 2000.
[2] "The USAF Stability and Control Digital Datcom," U.S. Air Force Flight Dynamics Lab., AFFDL-TR-79-3032, Dayton, OH, 2003.
[3] "Estimation of Sideforce, Yawing Moment and Rolling Moment Derivatives Due to Rate of Roll for Complete Aircraft at Subsonic Speeds," Engineering Sciences Data Unit, ESDU 85010, London, June 1985.
[4] "Pitching Moment and Lift Force Derivatives Due to Rate of Pitch for Aircraft at Subsonic Speeds," Engineering Sciences Data Unit, ESDU 90010, London, 1990.
[5] Hall, R. M., Biedron, R. T., Ball, D. N., Bogue, D. R., Chung, J., Green, B. E., et al., "Computational Methods for Stability and Control (COMSAC): The Time Has Come," AIAA Atmospheric Flight Mechanics Conf. and Exhibit, AIAA Paper 2005-6121, 2005.
[6] Johnson, F. T., Tinoco, E. N., and Yu, N., "Thirty Years of Development and Application of CFD at Boeing Commercial Airplanes, Seattle," *Computers and Fluids*, Vol. 34, 2005, pp. 1115–1151. doi:10.1016/j.compfluid.2004.06.005
[7] Charlton, E. F., "Numerical Stability and Control Analysis Towards Falling-Leaf Prediction Capabilities of SPLITFLOW for Two Generic High-Performance Aircraft Models," NASA CR-1998-208730, 1998.
[8] Godfrey, A. G., and Cliff, E. M., "Direct Calculation of Aerodynamic Force Derivatives: A Sensitivity-Equation Approach," AIAA Paper 98-0393, 1998.
[9] Limache, A., and Cliff, E., "Aerodynamic Sensitivity Theory for Rotary Stability Derivatives," *Journal of Aircraft*, Vol. 37, 2000, pp. 676–683. doi:10.2514/2.2651
[10] Park, M. A., Green, L. L., Montgomery, R. C., and Raney, D. L., "Determination of Stability and Control Derivatives Using Computational Fluid Dynamics and Automatic Differentiation," AIAA Paper 1999-3136, 1999.
[11] Park, M. A., and Green, L. L., "Steady-State Computation of Constant Rotational Rate Dynamic Stability Derivatives," AIAA Paper 2000-4321, 2000.
[12] Bischof, C., Khademi, P., Mauer, A., and Carle, A., "Adifor 2.0: Automatic Differentiation of Fortran 77 Programs," *Computational Science Engineering*, Vol. 3, No. 3, 1996, pp. 18–32. doi:10.1109/99.537089
[13] Green, L. L., and Spence, A. M., "Applications of Computational Methods for Dynamic Stability and Control Derivatives," AIAA Paper 2004-0377, 2004.
[14] Green, L. L., Spence, A. M., and Murphy, P. C., "Computational Methods for Dynamic Stability and Control Derivatives," AIAA Paper 2004-0015, 2004.
[15] Babcock, D. A., and Arena, A. S., "Estimating Aircraft Stability Derivatives Through Finite Element Analysis," AIAA Paper 2004-5174, Aug. 2004.
[16] Mialon, B., Khrabov, A., Ronch, A. D., Cavagna, L., Zhang, M., and Ricci, S., "Benchmarking the Prediction Of Dynamic Derivatives: Wind Tunnel Tests, Validation, Acceleration Methods," 28th AIAA Applied Aerodynamics Conf., Chicago, AIAA Paper 2010-8244, 2010.
[17] Roy, J.-F. L., and Morgand, S., "SACCON CFD Static and Dynamic Derivatives Using elsA," 28th AIAA Applied Aerodynamics Conf., Chicago, AIAA Paper 2010-4562, 2010.
[18] Ronch, A. D., Vallespin, D., Ghoreyshi, M., and Badcock, K., "Computation of Dynamic Derivatives Using CFD," 28th AIAA Applied Aerodynamics Conf., Chicago, AIAA Paper 2010-4817, 2010.
[19] Cummings, R. M., Jirásek, A., Petterson, K., and Schmidt, S., "SACCON Static and Dynamic Motion Flow Physics Simulation Using Cobalt," 28th AIAA Applied Aerodynamics Conf., Chicago, AIAA Paper 2010-4691, 2010.
[20] Tormalm, M., and Schmidt, S., "Computational Study of Static and Dynamic Vortical Flow over the Delta Wing SACCON Configuration Using the FOI Flow Solver Edge," 28th AIAA Applied Aerodynamics Conf., Chicago, AIAA Paper 2010-4561, 2010.
[21] Ronch, A. D., Ghoreyshi, M., Badcock, K., Görtz, S., Widhalm, M., Dwight, R., and Campobasso, M., "Linear Frequency Domain and Harmonic Balance Predictions of Dynamic Derivatives," 28th AIAA Applied Aerodynamics Conf., Chicago, AIAA Paper 2010-4699, 2010.
[22] Murman, S. M., "Reduced-Frequency Approach for Calculating Dynamic Derivatives," *AIAA Journal*, Vol. 45, No. 6, 2007, pp. 1161–1168. doi:10.2514/1.15758
[23] Mader, C. A., Martins, J. R. R. A., Alonso, J. J., and Van der Weide, E., "ADjoint: An Approach for the Rapid Development of Discrete Adjoint Solvers," *AIAA Journal*, Vol. 46, No. 4, 2008, pp. 863–873. doi:10.2514/1.29123
[24] Warsi, Z., *Fluid Dynamics: Theoretical an Computational Approaches*, Taylor & Francis, 3rd ed., Philadelphia, 2006.
[25] Ghosh, A. R., "Solution to Three-Dimensional Thin-Layer Navier–Stokes Equations in Rotating Coordinates for Flow Through Turbomachinery," M.S. Thesis, Mississippi State Univ., Starkville, MS, 1996.
[26] Van der Weide, E., Kalitzin, G., Schluter, J., and Alonso, J. J., "Unsteady Turbomachinery Computations Using Massively Parallel Platforms," 44th AIAA Aerospace Sciences Meeting and Exhibit, Reno, NV, AIAA Paper 2006-0421, 2006.
[27] Limache, A. C., "Aerodynamic Modeling Using Computational Fluid Dynamics and Sensitivity Equations," Ph.D. Thesis, Virginia Polytechnic Inst. and State Univ., Blacksburg, VA, 2000.
[28] Mader, C. A., and Martins, J. R. R. A., "Stability-Constrained Aerodynamic Shape Optimization of a Flying Wing Configuration," 13th AIAA/ISSMO Multidisciplinary Analysis and Optimization Conf., Fort Worth, TX, AIAA Paper 2010-9199, 2010.
[29] Martins, J. R. R. A., Sturdza, P., and Alonso, J. J., "The Complex-Step Derivative Approximation," *ACM Transactions on Mathematical Software*, Vol. 29, No. 3, 2003, pp. 245–262. doi:10.1145/838250.838251
[30] "Experimental Data Base for Computer Program Assessment," AGARD, AR-138, Neuilly-sur-Seine, France, May 1979.
[31] Ashby, D. L., "Potential Flow Theory and Operation Guide for the Panel Code PMARC," NASA TM-1999-209582, 1999.
[32] Balay, S., Buschelman, K., Eijkhout, V., Gropp, W. D., Kaushik, D., Knepley, M. G., et al., "PETSc Users Manual," Argonne National Lab., TR ANL-95/11, Rev. 2.1.5, Argonne, IL, 2004.

W. Anderson
Associate Editor